Available online at www.sciencedirect.com
ScienceDirect
Trans. Nonferrous Met. Soc. China 34(2024) 1681−1693
Transactions of Nonferrous Metals Society of China
www.tnmsc.cn

Electrochemical mechanism and kinetics of electrodissolution-coupled hafnium alkoxide synthesis in tetraethylammonium-chloride-based anhydrous system

Shuai LI[1], Sheng-hai YANG[1], Yong-ming CHEN[1], Chao-bo TANG[1], Yan-qing LAI[1], Chao-yong DENG[2], Chang-hong WANG[1]

1. School of Metallurgy and Environment, Central South University, Changsha 410083, China;
2. Ximei Resources Limited Company, Qingyuan 513000, China

Received 22 November 2022; accepted 20 March 2023

Abstract: Electrodissolution-coupled hafnium alkoxide synthesis (EHS) is a promising pathway for efficient electro-synthesis. It employs simultaneous heterogeneous reactions of Hf dissolution and ethanol dehydrogenation, and spontaneous solution-based combination reaction between Hf^{4+} cations and alkoxy anions. To elucidate the mechanism and kinetics of EHS process, the electrochemical behaviors of anodic Hf dissolution and cathodic ethanol dehydrogenation were explored through electrochemical measurements, SEM observations, gas chromatography, and micro-kinetics modeling. The results indicated the supporting electrolytes of tetraethylammonium chloride (Et_4NCl) to be preferable, which facilitated a passive-film-punctured pitting mechanism for Hf dissolution and a two-stage dehydrogenation mechanism. Three indicators related to passive rate, sensitivity towards puncture of the passive film, and pitting rate were extracted to quantify the kinetics of passive puncture and Hf corrosion. Micro-kinetics models were developed to evaluate the Et_4NCl-based EHS process, which achieved electric energy requirements of 1.53−1.83 kW·h/kg $Hf(OC_2H_5)_4$.

Key words: hafnium alkoxide synthesis; tetraethylammonium chloride; hafnium dissolution; ethanol dehydrogenation; electrochemical mechanism; electrochemical impedance spectroscopy (EIS); micro-kinetics modelling

1 Introduction

Currently, the tunneling currents of silicon dioxide/silicon (SiO_2/Si)-based metal oxide semiconductor (MOS) devices increase exponentially as the thickness of SiO_2 approaches the atomic level, which seriously affects its durability and reliability. It significantly reduces its application scale in the semiconductor industry [1,2]. Therefore, it is urgent to replace SiO_2 through a new gate dielectric film with a capacitance equivalent thickness of sub-1nm and a new channel substrate with high mobility and low power consumption to meet the continuously reducing scale of semiconductor devices. High dielectric constant gate hafnium oxide (HfO_2)-based dielectrics covered on III−V compound semiconductors [3−6], such as indium gallium arsenide and indium phosphide, indium arsenide, are prioritized for next-generation large-scale semiconductor integration applications due to their advantages of good controllability, high stability, high dielectric constant and excellent compatibility [7]. As excellent precursors, hafnium alkoxides [$Hf(OR)_4$, R is alkyl] have successfully prepared HfO_2 by atomic layer deposition (ALD) [1,8], and compared with metal chlorides, $Hf(OR)_4$ has many desirable advantages, such as high reactivity, low

Corresponding author: Chang-hong WANG, Tel: +86-15084806289, E-mail: Chang-hong.Wang@csu.edu.cn
DOI: 10.1016/S1003-6326(24)66499-X

deposition temperature and no risk of chlorine pollution on thin films [2,9].

Halide synthesis is the dominant technology for thermally-driven synthesis of the $Hf(OR)_4$ [10], which is expressed mainly via the reaction of $HfCl_4+4ROH+4NH_3 \xrightarrow{C_6H_6} Hf(OR)_4+4NH_4Cl$. Besides the chemical synthesis process, the halide synthesis approach also includes halide preparation, solid waste filtration, and purification of crude $Hf(OR)_4$ by distillation. Although the traditional halide synthesis is the most mature for $Hf(OR)_4$ synthesis, its wide industrial deployment is seriously restricted by undesired environmental burden and inefficiency. The undesired environmental burden is caused by the NH_4Cl solid waste, toxic gases such as chlorine and benzene, as well as large carbon dioxide footprints [11]. The tedious steps, various side-products, and low thermal efficiency of the halide synthesis incur inefficiency and low yield of $Hf(OR)_4$ (less than 70%) [10].

To address the challenges of undesired environmental burden and inefficiency, we proposed a promising electrodissolution-coupled $Hf(OR)_4$ synthesis (EHS) system, which adopts anhydrous alcohol as a solvent and metal Hf as feedstock, for green and efficient electro-synthesis of $Hf(OR)_4$. The EHS process employs anodic Hf dissolution, cathodic alcohol dehydrogenation, and spontaneous combination reaction of Hf^{4+} with OR^- to achieve the electro-synthesis of $Hf(OR)_4$. The efficient metal dissolution inspires the scheme in the hydrometallurgical electro-refining area [12,13] and the green preparation of hydrogen gas in the renewable energy area [14,15]. Compared with the conventional thermal method, the EHS system has the environmental advantages of no solid waste, no toxic exhaust, and high efficiency. During the EHS process, only negative carbon side-product hydrogen [16] is collected with no generation of solid waste or toxic waste. The electron in the Faradaically-driven EHS process directly acts on the target material to accurately regulate the charge transfer, which promotes its efficient electro-synthesis.

In our previous works, we explored the electrochemical behaviors of the EHS process in the tetraethylammonium hydrogen sulfate (Et_4NHSO_4)-based system [17], and found that the efficient operation of the Et_4NHSO_4-based EHS process was severely hindered by the weak anodic hafnium dissolution/corrosion occurred inside the spontaneously-formed passive film. It indicated that the Et_4NHSO_4-based EHS process needed to address the challenge of inefficiency in the anodic process to make it technically-feasible. Fortunately, we found an excellent tetraethylammonium chloride (Et_4NCl)-based EHS system [18], and focused on investigating its technical viability and economic applicability. It successfully demonstrated waste-free and efficient production of high-purity Hf ethoxide [$Hf(OC_2H_5)_4$], indicating a significant advance in the sustainability and efficiency of the Et_4NCl-based EHS system over traditional thermally-driven $Hf(OR)_4$ synthesis and Et_4NHSO_4-based EHS synthesis. It is noted that the current work, as an important theoretical foundation for our above work [18], was significant in guiding the proof-of-concept operation of the Et_4NCl-based EHS system and revealed why the Et_4NCl-based EHS system efficiently operated and developed the micro-kinetics process models based on the chronoamperometry and chronopotentiometry to optimize the operation process.

In this work, we focused investigations on the electrochemical mechanism and kinetics of the Et_4NCl-based EHS process that used green ethanol and Hf metal as feedstocks, with results to offer guidance for practical production. Firstly, we explored the influence mechanism of supporting electrolytes on the EHS electrode processes through cyclic voltammetry (CV) and linear sweep voltammetry (LSV), combined with gas chromatography and SEM observations. This helped us identify the Et_4NCl as the preferable supporting electrolyte. Then, we investigated the mechanism and kinetics of the cathodic and anodic processes in the Et_4NCl-based EHS system by various electrochemical techniques, including chronoamperometric (CA), chronopotentiometry (CP), and electrochemical impedance spectroscopy (EIS). Finally, we construct validated micro-kinetics process models to estimate the performance for the Et_4NCl-based EHS cells. The obtained experimental and modeling results provided valuable enlightenment for the efficient operation of the EHS system.

2 Process description of EHS

The EHS system with ethanol and metal Hf as feedstocks is composed of the electro-synthesis

process for the preparation of crude $Hf(OR)_4$ and purification processes including atmospheric and vacuum distillations for the preparation of high-purity $Hf(OR)_4$ (Fig. 1). Firstly, the electro-synthesis of $Hf(OR)_4$ was performed to prepare crude $Hf(OR)_4$. Subsequently, the normal purification process was performed to distill and recycle the mixed solvent of ethanol and acetonitrile at atmospheric pressure, and then to distill and collect the high-purity $Hf(OR)_4$ at vacuum pressure.

The theoretical operation mechanism of the EHS system is shown in Fig. 2, which indicates the synergistic heterogeneous reactions of cathodic dehydrogenation, anodic hafnium dissolution, and solution-based combination reaction. Specifically, the anodic Hf is electro-dissolved into solution in the form of Hf^{4+} cations, via reaction (Reaction 1). Adsorbed ethanol (C_2H_5OH) is dehydrogenized to form $C_2H_5O^-$ anions and hydrogen gas (H_2), via Reaction 2. The Hf^{4+} cations and $C_2H_5O^-$ anions migrate to each other and spontaneously form hafnium ethoxide [$Hf(C_2H_5O)_4$], via Reaction 3.

$$Hf \rightarrow Hf^{4+}+4e \quad (1)$$

$$2C_2H_5OH+2e \rightarrow 2C_2H_5O^-+H_2\uparrow \quad (2)$$

$$Hf^{4+}+4C_2H_5O^- \rightarrow Hf(C_2H_5O)_4 \quad (3)$$

3 Experimental

3.1 Materials

All the reagents used in the experiment include ethanol (anhydrous grade, ≥99.5%), acetonitrile (anhydrous grade, ≥99.8%), tetraethylammonium chloride (Et_4NCl), and tetraethylammonium hydrogen sulfate (Et_4NHSO_4). They were purchased from Aladdin without further purification.

3.2 Electrochemical measurement

The electrochemical behaviors of the EHS system were measured by a typical three-electrode system. The working electrode used for the investigation of anodic behaviors was a hafnium wire sealed in a polytetrafluoroethylene rod with a diameter of 3 mm (working area 0.047 cm^2), while for the investigation of cathodic behaviors was a platinum (Pt, purity of 99.99%) sheet with an area of 0.07 cm^2. A Pt plate with an area of 1 cm^2 and a saturated calomel electrode (SCE) were used as auxiliary electrode and reference electrode, respectively. The electrochemical measurements were performed in a mixed electrolyte of ethanol and acetonitrile (volume ratio 1:1) containing Et_4NCl or Et_4NHSO_4 (0.02 to 0.10 mol/L).

Prior to each experiment, the working electrode was polished with metallographic sandpaper (coarse-P1200 to fine-P3500), and treated with ultrasonic device to remove loose adsorbed ions. Then, it was washed with anhydrous ethanol and wiped dry with mirror tissue. The electrodes were immersed in an electrolyte purged with high-purity nitrogen to remove dissolved oxygen until the open circuit potential was stable.

Cyclic voltammetry (CV) and linear sweep voltammetry (LSV) were measured at different scanning rates (1−50 mV/s), and the obtained results were corrected by IR drop compensation. The chronoamperometric measurements (CA) were

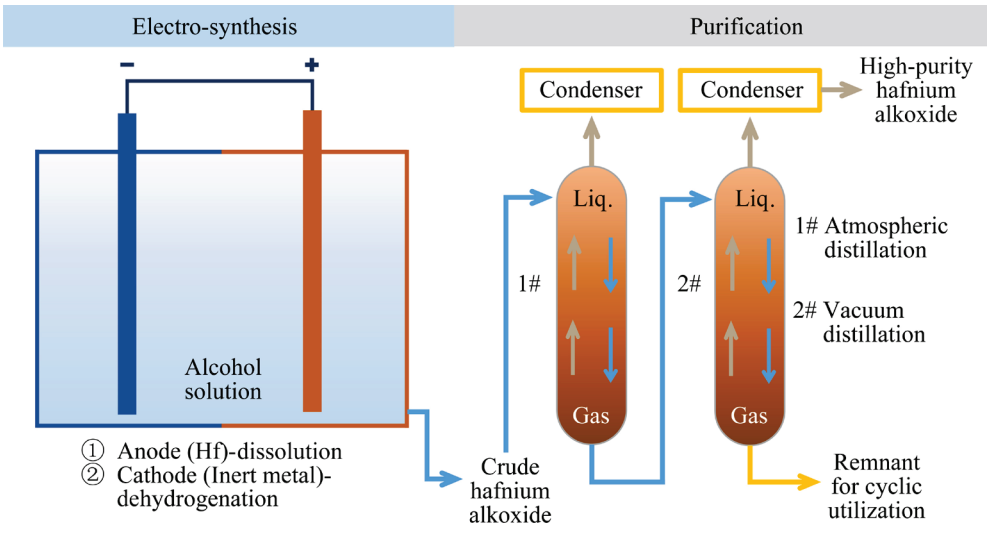

Fig. 1 Schematic flow diagram of EHS scheme for preparing high-purity $Hf(OR)_4$

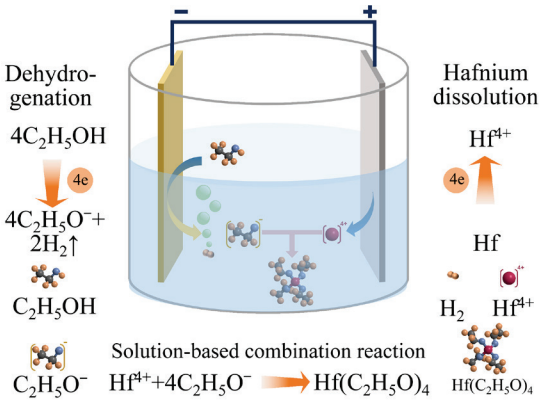

Fig. 2 Schematic of theoretical operation mechanism in EHS electro-synthesis process

obtained at different Et_4NCl concentrations and temperatures by constant potentials (1.6 to 4.0 V for anode, −1.6 to −0.5 V for cathode), while the chronopotentiometry (CP) was measured by continuous current densities (0.0015 to 7.5 mA/cm^2 for anode, −0.1 to −10 mA/cm^2 for cathode). The direct current measurements used in the experiment, such as CV, LSV, CA and CP, were performed by the CHI660E electrochemical workstation (Shanghai CH Instrument Company, China). Electrochemical impedance spectroscopy (EIS) was measured using Gamry Reference 600+ of 10 mV alternating current signal in the frequency range of 0.1 MHz to 0.1 Hz. The kinetics parameters of EIS were obtained by fitting all EIS spectra with the equivalent circuit in Gamry Echem Analyst. To investigate the corrosion mechanism of Et_4NCl and Et_4NHSO_4 systems, SEM (TESCAN Vega3 SBH) observations were used to analyze the surface morphology of Hf samples by chronoamperometry at 100 s under different potentials. The compositions of the collected gas samples after electrolysis at a current of 1.12 A for 68 h were analyzed by gas chromatography (GC-QP2010 Ultra) under the following conditions for electrolysis: anode plate of 11.6 cm × 8 cm; cathode plate of 14 cm × 8 cm; polar distance of 1 cm; cell size of 12 cm × 5 cm × 17 cm; 0.8 L mixed solvent of ethanol and acetonitrile (volume ratio 1:1); 0.06 mol/L supporting electrolyte (Et_4NCl or Et_4NHSO_4).

3.3 Numerical analysis of kinetic parameter

The relationship between pitting potential (φ_{pit}) and the square root of the scanning rate ($v^{1/2}$) was obtained by using the least square fitting program as follows [19,20]:

$$\varphi_{pit} = \sqrt{v/\alpha} + A \tag{4}$$

where v is the scanning rate; α and A are constants.

The $\lg J$–$\lg t$ relationship based on the chronoamperometry can be expressed as [21,22]

$$\lg J = A - m\lg t \tag{5}$$

$$\lg J = B + n\lg t \tag{6}$$

where J is the current density; B is the constant, m and n are the slopes of $\lg J$–$\lg t$, m represents the parameter related to passive rate, and n represents the parameter related to pit growth rate.

3.4 Micro-kinetic modeling

Based on the kinetics of anodic hafnium electro-dissolution and cathodic dehydrogenation of the EHS process extracted from CA and CP curves, the micro-kinetics modeling was carried out at different current densities. The cell potential difference ($\Delta\varphi$), solution potential drop ($\Delta\varphi_{sol}$), and anodic (φ_a) and cathodic (φ_c) potentials were calculated by the following equations [23]:

$$\Delta\varphi = \Delta\varphi_{sol} + (\varphi_a - \varphi_c),\ \Delta\varphi_{sol} = \frac{L_{pd}\cdot J_{ap}}{\sigma} \tag{7}$$

$$\varphi_a = \beta_a \lg J - \alpha_a,\ \beta_a = \frac{2.303\times 8.314T}{\alpha_0 zF} \tag{8}$$

$$\varphi_c = -\beta_c \lg J + \alpha_c,\ \beta_c = \frac{2.303\times 8.314T}{\beta_0 zF} \tag{9}$$

where L_{pd} is the polar distance and is set as 1 cm; J_{ap} is the applied current density; σ is the conductivity of electrolyte containing Et_4NCl; α_a and α_c are constants related to the anode and cathode, respectively; β_a and β_c are the Tafel slopes of anode and cathode, respectively; T is the temperature; z is the number of electrons involved in the electrode reaction; F is the Faraday constant, 96485 C/mol; α_0 and β_0 are the anodic and cathodic charge transfer coefficients, respectively.

We simulated the electrolysis process with the concentration of dissolved Hf^{4+} cation increasing from 0 to 200 g/L and estimated the required charge and theoretical amount of $Hf(OC_2H_5)_4$ synthesized in the EHS process. Thus, the modeled energy consumption (W_m) can be estimated through the following equation [18,24−26]:

$$W_m = \frac{\int_0^Q \Delta\varphi \,\mathrm{d}Q}{\Delta n_{Hf(OC_2H_5)_4}} \tag{10}$$

where Q is the charge involved in Faraday reactions; $\Delta n_{\mathrm{Hf(OC_2H_5)_4}}$ is the theoretical amount of $Hf(OC_2H_5)_4$ synthesized in the EHS process, which is calculated by the Q. The modeled electricity charge (C_m) is calculated based on the obtained W_m and average industrial electricity charge of 0.113 US$/(kW·h).

4 Results and discussion

4.1 Influence mechanism of supporting electrolytes

We firstly performed cyclic voltammetry (CV) and linear sweep voltammetry (LSV) combined with gas chromatography and SEM observations to explore the influence mechanism of two typical supporting electrolytes, tetraethylammonium chloride (Et_4NCl) and tetraethylammonium hydrogen sulfate (Et_4NHSO_4) on the electrochemical behaviors of EHS system, to identify the preferable electrolyte for the practical operation (Fig. 3).

The CV curves, complemented with the SEM images, reflects two types of anodic dissolution/corrosion mechanisms induced by the two supporting electrolytes.

Figure 3(a), complemented with Fig. 3(c), reflects an efficient pitting mechanism of the anodic Hf dissolution in the Et_4NCl system. Specifically, Fig. 3(a) shows that with scanning potential towards a positive value, the current density is at a low level within an extended passivation region. This is due to the spontaneously-formed passive film of hafnium oxide (HfO_2) on the electrode surface [27]. With potential reaching a critical value denoted as pitting potential (φ_{pit}), the current density gradually increases rapidly, indicating a gradual puncture on passive film and initiation and propagation of corrosion on bare Hf [27]. After scanning reversal, current density returns to the low level and forms an apparent anticlockwise hysteresis loop, a typical feature of pitting corrosion [28]. The SEM observations (Fig. 3(c)) confirm the pitting. Note that with increasing potential scanning rate (v) from 1 to 50 mV/s, the φ_{pit} shifts to a more positive value. To quantify this phenomenon, we constructed the mathematical relationship between φ_{pit} and $v^{1/2}$ via Reaction (1) and obtained a numerical model of $\varphi_{pit}=2.48v^{1/2}+3.18$ with the correlation coefficient (r^2) of 0.98 (Fig. S1, in supplementary materials, SM). This result can be explained by incubation time [29], which is shorter at a higher scanning rate due to the shorter time to puncture the passive film and induce the pitting corrosion. In other words, at lower scanning rates, puncture of the passive film

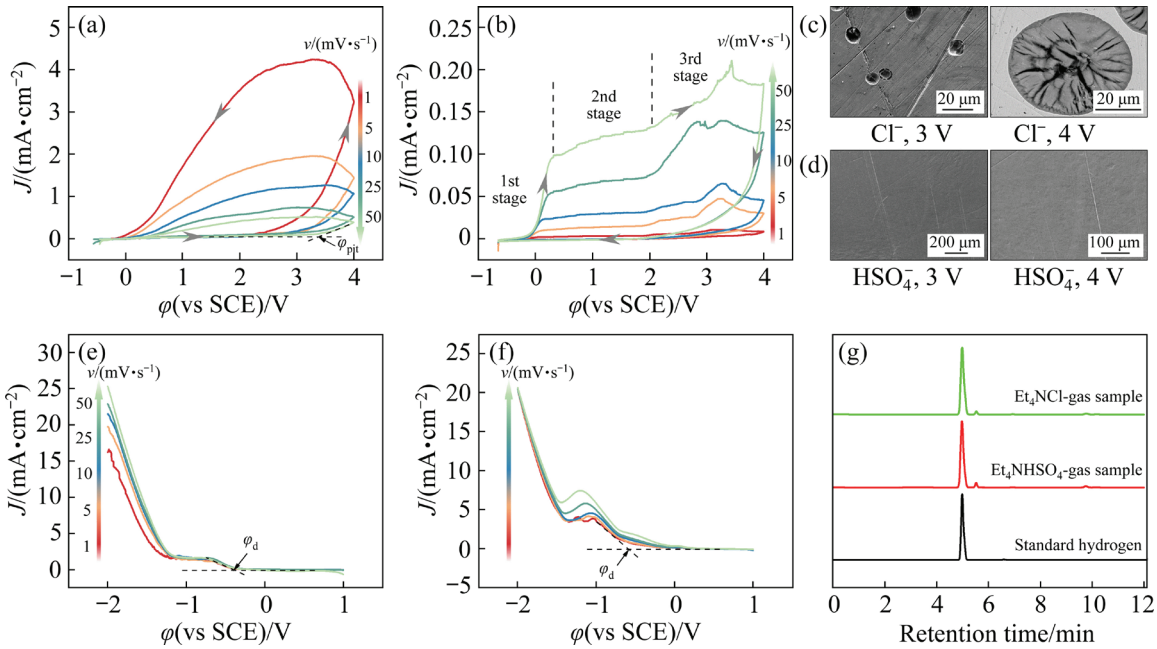

Fig. 3 Influence mechanism of supporting electrolytes (Et_4NCl or Et_4NHSO_4) on EHS electrode process: Cyclic voltammetry curves on Hf at different scanning rates in Et_4NCl (a) or Et_4NHSO_4 (b) system; SEM images of Et_4NCl (c) or Et_4NHSO_4 (d) system; Linear sweep voltammetry curves in Et_4NCl (e) or Et_4NHSO_4 (f) system; Gas chromatography of collected gas sample after electrolysis (g)

and pitting corrosion of the bare Hf can be sufficiently achieved with enough incubation time.

Figure 3(b), complemented with Fig. 3(d), reflects a weak corrosion mechanism under passive film in the Et_4NHSO_4 system. Specifically, Fig. 3(b) shows that with scanning potential toward positive value, the current density passes through three stages: transition, passivation, and trans-passivation. The transition stage exhibits a rapid increase of current density to a nearly stable value. The passivation stage shows a weak increase in current density, which is attributed to the dissolution/corrosion of Hf under the spontaneously formed porous passive film and the diffusion of dissolved Hf^{4+} cations into the electrolyte solution through the passive film pores [17]. The trans-passivation stage shows a sudden increase again in current density. After scanning reversal, the current density returns without an anticlockwise hysteresis loop. The overall current density is at a low level because of the high resistance of the porous passive film to the diffusion of dissolved Hf^{4+} cations. Figure 3(d) confirms the weak corrosion under the passive film. The current densities within the passivation stage were extracted to construct a relationship with $v^{1/2}$, presenting linear relations (Fig. S2 in SM). It confirms that Et_4NHSO_4 contributes to the corrosion under passive film with Hf^{4+} diffusion within the pores as the controlled step. Comparing the above two systems, we conclude that the Hf dissolution/corrosion is thermodynamically and kinetically easier to induce in the Et_4NCl system than in the Et_4NHSO_4.

The LSV curves (Figs. 3(e, f)), complemented with the gas chromatography (Fig. 3(g)), reflect a two-stage dehydrogenation reaction mechanism in both the Et_4NCl and Et_4NHSO_4 systems [30]: At the first stage, with the potential scanning to a typical value, denoted as dehydrogenation potential (φ_d), the gas bubble appears due to dehydrogenation of the ethanal adsorbed on the electrode surface with hydrogen evolution. With continuing to scan potential, the bubble releases gradually become intense, owing to the increasing overpotential that drives the dehydrogenation reaction. In the second stage, the current density increases more rapidly with decreasing applied potential compared to the first stage. This indicates a transition to dehydrogenation mode, and the second stage is more desirable for the practical operation of the EHS cathode process. Figure 3(g) confirms the evolution gas to be hydrogen gas, demonstrating the dehydrogenation reaction mechanism. Despite scanning at different rates for the two systems, the shape and trend of LSV curves do not change radically, indicating little influence on the two-stage dehydrogenation reaction mechanism. The dehydrogenation processes of the two systems are thermodynamically and kinetically acceptable.

Overall, the above results provide a meaningful comparison between Et_4NCl and Et_4NHSO_4 and help us identify the Et_4NCl system as the preferable one, in which the thermodynamically possible and kinetically-efficient hafnium dissolution and ethanol dehydrogenation can be achieved at appropriate potentials. It also demonstrates the theoretical operation mechanism in Fig. 2.

4.2 Cathodic behavior of Et_4NCl-based EHS

After determining Et_4NCl as the suitable supporting electrolyte, we further explored the cathodic dehydrogenation behaviors at the constant cathodic potential in the Et_4NCl-based EHS system (Fig. 4), with results to guide its practical operation. Figure 4(a) shows that, at relatively positive applied potentials (φ_{ap}) from −0.4 to 0.5 V, the current density rapidly approaches nearly zero. It indicates that these applied potentials are insufficient to trigger a cathodic dehydrogenation reaction. On the other hand, with φ_{ap} from −0.8 to −1.6 V, the current density decreases rapidly to a steady-state value (J_{ss}), accompanied by many bubbles released around the electrode surface. This indicates occurrence of the ethanol dehydrogenation reaction. The rapid decrease region of current density is attributed to the charging process, while the J_{ss} region is assigned to stable ethanol dehydrogenation with hydrogen gas (H_2) releasing. These are consistent with the LSV results that beyond φ_h, and the dehydrogenation occurs with the evolution of H_2.

Note that the shifting φ_{ap} towards a negative value and increasing Et_4NCl concentration (Fig. 4(b)) and the temperature (Fig. 4(c)) enhances the J_{ss}, indicating improvements in the kinetics of the cathodic dehydrogenation process. To quantify the influence of these three factors on the kinetics, we extracted the J_{ss} and constructed their relationships with three factors (Fig. S3 in SM), presenting linear

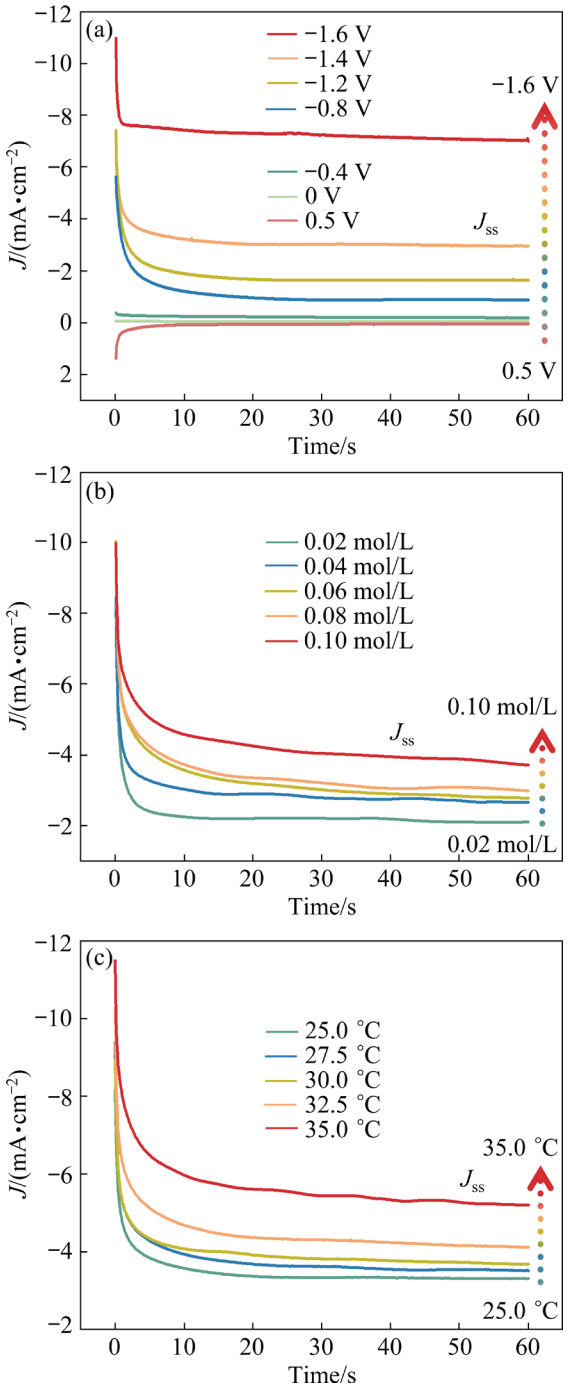

Fig. 4 Curves of cathodic transient current density vs time obtained by chronoamperometry at different cathodic potentials (a), different concentrations of Et_4NCl (b), and different temperatures (c)

relations. The numerical models are as follows: for the factor of φ_{ap}, $\lg J_{ss}=-1.33\varphi_{ap}-1.30$ with R^2 of 0.98; for the Et_4NCl concentration (C), $\lg J_{ss}=2.96C+0.27$ with R^2 of 0.99; for the temperature (T), $\lg J_{ss}=0.01T+0.17$ with R^2 of 0.96. These numerical models construct the mathematical relationship between operation conditions, such as φ_{ap}, C, and T and cathodic kinetics (J_{ss}). Using these, we can deduce the kinetics performance at the φ_{ap}, C, and T beyond the values in this work, which guides the practical cathodic operation of EHS.

Then, we investigated the cathodic dehydrogenation behaviors at constant current density in the Et_4NCl-based EHS system, with results to guide its practical operation (Fig. 5). Despite different applied current densities (−0.1 to −10 mA/cm^2), the applied potentials increase to a stable plateau (φ_{ss}), reflecting a transition from the charging process within the double layer into the cathodic dehydrogenation process. The φ_{ss} of −0.35 V at 0.1 mA/cm^2 corresponds to the φ_d in LSV curve, which indicates a thermodynamic initiation of dehydrogenation reaction. With decreasing current density from −0.1 to −10 mA/cm^2, φ_{ss} shifts from −0.35 to −1.89 V owing to the Butler–Volmer equation [31]. Higher applied current density requires higher overpotential as a driving force to match the required kinetics property. To quantify the effect of J_{ap} on the kinetics of the dehydrogenation process, we constructed the dependence of φ_{ss} on J_{ap} (Fig. S4 in SM): $\varphi_{ss}=-0.57J_{ap}^{1/2}-0.21$ with R^2 of 0.95. Using this model, we can deduce the kinetics performance at the J_{ap} beyond the values in this work, which guides the practical cathodic operation of EHS.

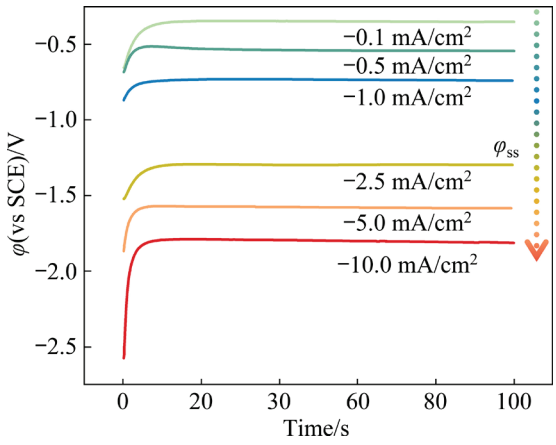

Fig. 5 Curves of cathodic transient potential vs time obtained by chronopotentiometry

4.3 Anodic behaviors of Et_4NCl-based EHS

We investigated the anodic behaviors of passive film puncture and Hf dissolution/corrosion at the constant anodic potential in the Et_4NCl-based EHS system, with results to guide its practical operation (Fig. 6). Figure 6(a) shows that at applied

potential (φ_{ap}) from 1.6 to 2 V, the current density decreases to a nearly 0, which reflects the process of formation, growth, and compactification of the passive film. On the other hand, with φ_{ap} from 2.8 to 4.0 V, the current density rapidly decreases to a minimum value in an induction period (t_0) due to the formation and growth of the passive film. It then increases due to the passive film's puncture and the pitting's initiation and growth on the bare Hf.

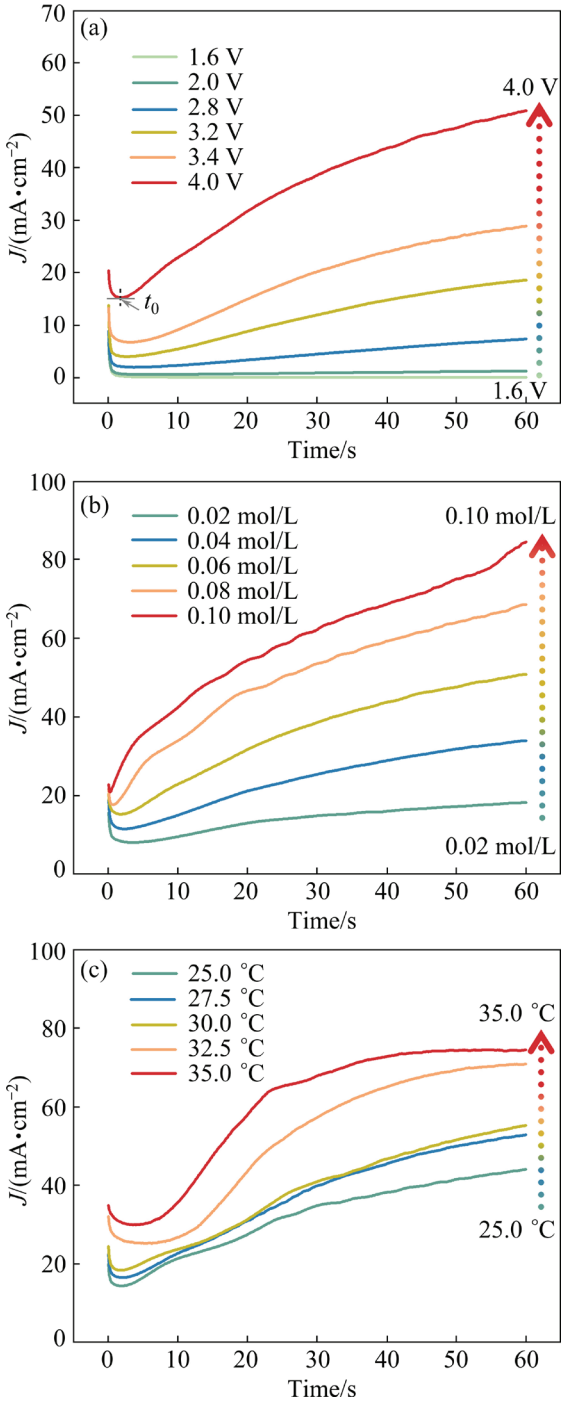

Fig. 6 Curves of anodic transient current density vs time obtained by chronoamperometry at different anodic potentials (a), different concentrations of Et_4NCl (b), and different temperatures (c)

Evidently, increasing the φ_{ap}, Et_4NCl concentration, and temperature does not change the shape and trend of the J–t curves but increases the overall current density. It indicates no radical change in the anodic mechanism and improvements in the kinetics of the passive puncture and Hf dissolution. To quantify the effect of the three factors on the kinetics, we converted the J–t curves into the logarithmic scale (Fig. S5 in SM) and extracted the $|m|$ (related to passive rate), n (related to pit growth rate) and the incubation time (t_0, related to sensitivity towards puncture of the passive film) based on Eqs. (5) and (6), which are recorded in Tables S1−S3 in SM. As the φ_{ap} increases from 1.6 to 4.0 V, $|m|$ decreases from 0.77 to 0.12, n increases from 0.40 to 0.74, and t_0 decreases from 24.00 to 1.80 s. It indicates that higher applied potential reduces the passive rate, increases the pit growth rate, and improves the puncture sensitivity of the passive film. Furthermore, Et_4NCl concentration and temperature factors show almost the same effect on the anodic passive film puncture and Hf corrosion. However, increasing applied potential, Et_4NCl concentration, and temperature to excessive values would incur side reactions, and bring pressure on the cyclic utilization of solid Et_4NCl and impair the stability. Therefore, the stable and efficient anodic operation of EHS requires appropriately applied potential, Et_4NCl concentration, and temperature.

Then, we further investigated the anodic behaviors of the anodic passive puncture and Hf corrosion at constant current density in the Et_4NCl-based EHS system to guide its practical operation (Fig. 7). At J_{ap} of 0.0015 mA/cm^2, the applied potential gradually increases to a steady value due to the formation and growth of the passive film. It indicates that the applied current density is insufficient to trigger the passive film puncture and subsequent pitting of the bare Hf. At J_{ap} of 0.75−7.5 mA/cm^2, the applied potential increases to a maximum (φ_{max}) due to the formation and growth of the passive film, and then decreases to a steady state value (φ_{ss}) due to puncture of the passive film and growth of pitting corrosion. The φ_{max} indicates the competition between the growth of passive film and its puncture, while φ_{ss} indicates stable pitting corrosion. To quantify the effect of J_{ap}

on the kinetics of the pitting corrosion, we constructed the dependence of φ_{ss} on J_{ap} (Fig. S6 in SM): φ_{ss}=0.53lgJ_{ap}+2.09 with R^2 of 0.99. With increasing J_{ap} from 0.75 to 7.5 mA/cm^2, φ_{ss} shifts from 1.93 to 2.63 V. Higher applied current density requires higher overpotential as a driving force to maintain pitting corrosion based on the Butler–Volmer equation [31]. Despite the promotion of J_{ap} on the puncture of the passive film and pitting corrosion on Hf, the J_{ap} should not be too high to avoid possible side-reactions. Therefore, to ensure a stable and efficient anodic operation of the EHS process, an appropriate J_{ap} is required.

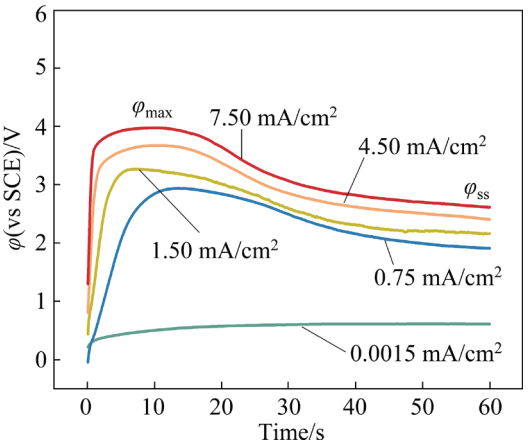

Fig. 7 Curves of anodic transient potential vs time obtained by chronopotentiometry

To clarify the charge transfer kinetics of the anodic passive film removal and Hf dissolution in the Et$_4$NCl-based EHS system, we explored the electrochemical impedance spectroscopy at different Et$_4$NCl concentrations (Fig. 8(a)). In the higher-frequency region, the semicircle reflects the characteristic of charge transfer of Hf corrosion with the presence of the passive film. The intersection of the semicircle with the real axis at a higher frequency represents the solution resistance. At the lower-frequency region, the "Warburg tail" represents the diffusion characteristics of dissolved Hf^{4+} cation within the passive film. Combined with the Bode diagram (Fig. S7 in SM), the Nyquist spectra show two time-constants in the high-frequency and low-frequency regions, respectively.

The Nyquist data were fitted through a typical equivalent circuit (Fig. 8(b)), which consisted of internal resistance R_Ω (electrolyte solution resistance R_s), Faraday impedance Z_f (polarization resistance related to charging transfer process R_P and Warburg impedance reflecting the dissolved Hf^{4+} in the passivation film hole W), and double-layer capacitance C_d (constant-phase element used to replace the pure double-layer capacitor with high fitting accuracy [32], CPE, Q_{if}).

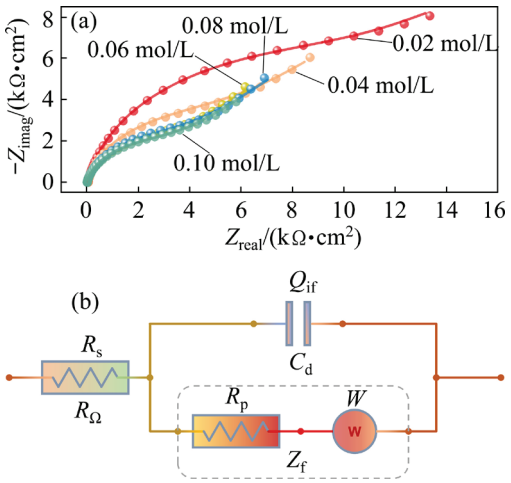

Fig. 8 Nyquist plots of EIS in Et$_4$NCl-based EHS system (a), and equivalent circuit used for fitting EIS spectrum based on electrochemical process of Et$_4$NCl-based EHS system (b)

The fitting results are recorded in Table 1, and their goodness of fit (R^2) based on the equivalent circuit (Fig. 8(b)) is more significant than 0.99, indicating their validity. Table 1 shows that Et$_4$NCl concentration from increases 0.02 to 0.10 mol/L and R_s decreases from 53.39 to 13.36 Ω·cm^2 due to the Et$_4$NCl-driven increasing conductivity. As Et$_4$NCl concentration increases from 0.02 to 0.10 mol/L, R_p decreases from 10402.00 to 3215.10 Ω·cm^2, W and Y_0 increase from 7.00×10^{-7} s$^{1/2}$/(Ω·cm^2) and 1.09×10^{-7} s$^{\alpha}$/(Ω·cm^2) to 1.21×10^{-6} s$^{1/2}$/(Ω·cm^2) and 1.50×10^{-7} s$^{\alpha}$/(Ω·cm^2), while the values of α close to 1 represent the CPE acting as a capacitive element. This is because higher bulk Et$_4$NCl concentration results in its higher local concentration corresponding increase in diffusion resistance, but on the other hand this facilitates more adsorption of Cl^- anion on the passive film and its chemical removal [33,34]. Overall, the R_p at 2.0 V and range of 0.02−0.10 mol/L Et$_4$NCl is high, indicating that the passive film has not been punctured and the Hf corrosion undergoes under it. It is consistent with the CV and CA results that a high overpotential is required to puncture the passive film and induce the bare Hf dissolution. However, excessively high overpotentials would trigger possible side reactions

and incur inefficiency of the EHS anodic process. Therefore, an appropriate applied potential is required to ensure efficient EHS anode operation.

Combining results of the cathodic and anodic behaviors, we gained important insights into the EHS operation: (1) Modulating the applied potential or current density, Et_4NCl concentration, and temperature at appropriate values is required to ensure efficient puncture of the passive film and dissolution of the bare Hf as well as efficient dehydrogenation. It is essential to avoid the low-current-density inefficiency and high-current-density inefficiency with undesired side-reactions and poor Faradaic efficiency, which achieves a thermodynamically and kinetically desirable EHS electrolysis; (2) The cathodic and anodic processes are required to be kinetically balanced, to ensure kinetics-symmetric electrode reactions. It is essential to facilitate waste-free and efficient operation. Therefore, in the practical EHS operation, we should grasp the trade-off that facilitates cathodic and anodic processes kinetically efficient and mutually coordinated.

4.4 Micro-kinetics modeling of Et_4NCl-based EHS

Based on the kinetics of CA and CP results for cathodic dehydrogenation and anodic Hf dissolution processes of Et_4NCl-based EHS, we constructed their micro-kinetics process model based on Eqs. (4)−(6) and evaluated their micro-energy consumption based on Eq. (7), with results to guide optimization of EHS operation. Table 2 shows that the modeled electric energy requirements (W_m) calculated based on CA and CP results are very close, indicating the high reliability of micro-kinetics modeling. With increasing current density from 50 to 75 A/m^2, the W_m increases from 1.53−1.55 kW·h/kg $Hf(OC_2H_5)_4$ to 1.81−1.83 kW·h/kg $Hf(OC_2H_5)_4$, while the C_m increases from 0.17−0.18 US$/kg $Hf(OC_2H_5)_4$ to 0.20−0.21 US$/kg $Hf(OC_2H_5)_4$. It indicates efficient EHS electrolysis. This result is directly associated with the cell potential drop, which increases from 5.12−5.17 V to 6.06−6.12 V, due to the effects of current density on the overpotential based on the Butler−Volmer law [31] and the solution potential drop based on the Ohm's law [35].

To validate the micro-kinetics process model, we carried out the bench-scale operation of Et_4NCl-based EHS electrolysis experiments, demonstrating its reliability [18]. The model could optimize experiment conditions, such as current density, solution temperature, and polar distance, which could save the experimental investment.

5 Conclusions

(1) The results indicated a robust pitting mechanism with the puncture of the passive film for the Hf dissolution process in the Et_4NCl system, while a weak corrosion mechanism was shown under the passive film in the Et_4NHSO_4 system. Both systems of Et_4NCl and Et_4NHSO_4 indicated a

Table 1 Anodic charge transfer kinetics parameters of Et_4NCl-based EHS system

C/(mol·L^{-1})	R_s/(Ω·cm^2)	R_p/(Ω·cm^2)	Y_0/(s$^{\alpha}$·Ω^{-1}·cm^{-2})	α	W/(s$^{1/2}$·Ω^{-1}·cm^{-2})	R^2
0.02	53.39	10402.00	1.09×10^{-7}	0.91	7.00×10^{-7}	0.99
0.04	29.33	5275.90	1.30×10^{-7}	0.91	8.57×10^{-7}	0.99
0.06	21.02	3311.00	1.40×10^{-7}	0.91	1.05×10^{-6}	0.99
0.08	15.84	3273.90	1.46×10^{-7}	0.90	1.17×10^{-6}	0.99
0.10	13.36	3215.10	1.50×10^{-7}	0.90	1.21×10^{-6}	0.99

Table 2 Micro-kinetics modeling parameters in Et_4NCl-based EHS process

Technique	φ(vs SCE)/V	φ_c(vs SCE)/V	$\Delta\varphi_{sol}$(vs SCE)/V	$\Delta\varphi$(vs SCE)/V	W_m/(kW·h·kg^{-1})	C_m/(US$·kg^{-1})
CA, 50 A/m^2	2.62	−1.52	1.03	5.17	1.55	0.18
CP, 50 A/m^2	2.51	−1.58	1.03	5.12	1.53	0.17
CA, 75 A/m^2	2.93	−1.64	1.55	6.12	1.83	0.21
CP, 75 A/m^2	2.82	−1.69	1.55	6.06	1.81	0.20

two-stage dehydrogenation reaction mechanism. The Et_4NCl system was preferable for the thermodynamically viable and kinetically-efficient operation of the EHS process.

(2) The result of cathodic dehydrogenation behaviors for the Et_4NCl-based EHS process revealed the numerical models that quantified the dehydrogenation kinetics: For the applied potential (φ_{ap}), $\lg J_{ss}=-1.33\varphi_{ap}-1.30$ with R^2 of 0.98; For the Et_4NCl concentration (C), $\lg J_{ss}=2.96C+0.27$ with R^2 of 0.99; For the temperature (T), $\lg J_{ss}=0.01T+0.17$ with R^2 of 0.96.

(3) The result of anodic pitting behavior for the Et_4NCl-based EHS process revealed the typical indicators, which quantified the kinetics of the passive puncture and Hf corrosion, of $|m|$ (related to passive rate), n (related to pit growth rate) and the incubation time (t_0, related to sensitivity towards puncture of the passive film). As the anodic potential increased from 1.6 to 4.0 V, $|m|$ decreased from 0.77 to 0.12, n increased from 0.40 to 0.74, and t_0 decreased from 24.00 to 1.80 s. It indicated that higher applied potential reduced the passive rate, increased the pit growth rate, and improved the puncture sensitivity of the passive film.

(4) The above results gained insights into the practical operation of the Et_4NCl-based EHS: Modulating the applied potential, or current density, Et_4NCl concentration, and temperature at appropriate values benefited efficient dehydrogenation, efficient puncture of the passive film, dissolution of the bare Hf, as well as kinetically balanced cathodic and anodic processes.

(5) Micro-kinetics process models were developed to analyze the Et_4NCl-based EHS electrolysis based on chronoamperometry and chronopotentiometry, which were validated by the practical bench-scale operation [18]. The micro-kinetics modeling achieved an electric energy requirement of 1.53−1.83 kW·h/kg $Hf(OC_2H_5)_4$ and an electric charge of 0.17−0.21 US$/kg $Hf(OC_2H_5)_4$.

CRediT authorship contribution statement

Shuai LI: Investigation, Formal analysis, Writing − Original draft; **Sheng-hai YANG:** Resources, Funding acquisition; **Yong-ming CHEN:** Funding acquisition; **Chao-bo TANG:** Funding acquisition; **Yan-qing LAI:** Funding acquisition; **Chao-yong DENG:** Funding acquisition; **Chang-hong WANG:** Conceptualization, Methodology, Writing − Reviewing and editing, Funding acquisition, Supervising.

Declaration of competing interest

The authors declare that they have no known competing financial interests or personal relationships that could have appeared to influence the work reported in this paper.

Acknowledgments

This work was supported by the Science and Technology Innovation Program of Hunan Province, China (No. 2021RC2002), and the Yangfan Plan, China (No. 2017YT05C107).

Supplementary materials

Supplementary materials in this paper can be found at: http://tnmsc.csu.edu.cn/download/23-p1681-2022-1336-Supplementary_Materials.pdf.

References

[1] GORDON R G, BECKER J, HAUSMANN D, SUH S. Vapor deposition of metal oxides and silicates: Possible gate insulators for future microelectronics [J]. Chemistry of Materials, 2001, 13: 2463−2464.

[2] MUI C, MUSGRAVE C B. Atomic layer deposition of HfO_2 using alkoxides as precursors [J]. The Journal of Physical Chemistry B, 2004, 108: 15150−15164.

[3] SUZUKI R, TAOKA N, YOKOYAMA M, LEE S, KIM S H, HOSHII T, YASUDA T, JEVASUWAN W, MAEDA T, ICHIKAWA O, FUKUHARA N, HATA M, TAKENAKA M, TAKAGI S. 1-nm-capacitance-equivalent-thickness HfO_2/Al_2O_3/InGaAs metal-oxide-semiconductor structure with low interface trap density and low gate leakage current density [J]. Applied Physics Letters, 2012, 100: 132906.

[4] KANG Y S, KIM C Y, CHO M-H, CHUNG K B, AN C-H, KIM H, LEE H J, KIM C S, LEE T G. Thickness dependence on crystalline structure and interfacial reactions in HfO_2 films on InP (001) grown by atomic layer deposition [J]. Applied Physics Letters, 2010, 97: 172108.

[5] KANG Y S, KIM C Y, CHO M H, AN C H, KIM H, SEO J H, KIM C S, LEE T G, KO D H. Interfacial reactions between HfO_2 films prepared by atomic-layer-deposition and an InP substrate using postnitridation with NH_3 vapor [J]. Electrochemical and Solid-State Letters, 2012, 15: G9.

[6] ZHANG S B, NORTHRUP J E. Chemical potential dependence of defect formation energies in GaAs: Application to Ga self-diffusion [J]. Physical Review Letters, 1991, 67: 2339−2342.

[7] TIMM R, HEAD A R, YNGMAN S, KNUTSSON J V, HJORT M, MCKIBBIN S R, TROIAN A, PERSSON O, URPELAINEN S, KNUDSEN J, SCHNADT J,

MIKKELSEN A. Self-cleaning and surface chemical reactions during hafnium dioxide atomic layer deposition on indium arsenide [J]. Nature Communications, 2018, 9: 1412.

[8] HAUSMANN D M, KIM E, BECKER J, GORDON R G. Atomic layer deposition of hafnium and zirconium oxides using metal amide precursors [J]. Chemistry of Materials, 2002, 14: 4350−4358.

[9] MIIKKULAINEN V, LESKELÄ M, RITALA M, PUURUNEN R L. Crystallinity of inorganic films grown by atomic layer deposition: Overview and general trends [J]. Journal of Applied Physics, 2013, 113: 021301.

[10] BRADLEY D C, MEHROTRA R C, ROTHWELL I P, SINGH A. Alkoxo and Aryloxo Derivatives of Metals [M]. Amsterdam: Elsevier, 2001: 445−669.

[11] ARTZ J, MÜLLER T E, THENERT K, KLEINEKORTE J, MEYS R, STERNBERG A, BARDOW A, LEITNER W. Sustainable conversion of carbon dioxide: An integrated review of catalysis and life cycle assessment [J]. Chemical Reviews, 2018, 118: 434−504.

[12] PENG Rong-qiu. Metallurgy of heavy metals [M]. Changsha: Central South University Press, 2004. (in Chinese)

[13] LI You-gang, LIU Shan-shan, WANG Chang-hong, LUO Tao, XIANG Chang-liu, LI Shuai, CHANG Cong, YANG Sheng-hai, WANG Heng-hui, CHEN Yong-ming. Electro-deposition behavior in methanesulfonic-acid-based lead electro-refining [J]. Journal of Sustainable Metallurgy, 2021, 7: 1910−1916.

[14] TURNER J A. A realizable renewable energy future [J]. Science, 1999, 285: 687−689.

[15] GLENK G, REICHELSTEIN S. Economics of converting renewable power to hydrogen [J]. Nature Energy, 2019, 4: 216−222.

[16] SHARIFIAN R, WAGTERVELD R M, DIGDAYA I A, XIANG Cheng-xiang, VERMAAS D A. Electrochemical carbon dioxide capture to close the carbon cycle [J]. Energy & Environmental Science, 2021, 14: 781−814.

[17] LI Shuai, YANG Sheng-hai, WANG Chang-hong. Electrochemical behavior of tetraethylammonium-hydrogen sulfate-based electrodissolution-coupled hafnium alkoxide synthesis [J]. JOM, 2022, 74: 3548−3556.

[18] LI Shuai, YANG Sheng-hai, LI Kang-kang, LAI Yan-qing, DENG Chao-yong, WANG Chang-hong. Electrodissolution-coupled hafnium alkoxide synthesis with high environmental and economic benefits [J]. ChemSusChem, 2022, 15: e202200474.

[19] BASTIDAS J M, POLO J L, TORRES C L, CANO E. A stochastic approach to study localized corrosion of AISI 304L and AISI 316L stainless steels as a function of potential scan rate [J]. Corrosion, 2001, 57: 666−669.

[20] SHIBATA T. Stochastic studies of passivity breakdown [J]. Corrosion Science, 1990, 31: 413−423.

[21] LIN L F, CHAO C Y, MACDONALD D D. A point defect model for anodic passive films: II. Chemical breakdown and pit initiation [J]. Journal of the Electrochemical Society, 1981, 128: 1194−1198.

[22] AMIN M A. Uniform and pitting corrosion events induced by SCN− anions on Al alloys surfaces and the effect of UV light [J]. Electrochimica Acta, 2011, 56: 2518−2531.

[23] KÖTZ R, CARLEN M. Principles and applications of electrochemical capacitors [J]. Electrochimica Acta, 2000, 45: 2483−2498.

[24] WANG Chang-hong, JIANG Kai-qi, JONES T W, YANG Sheng-hai, YU Hai, FERON P, LI Kang-kang. Electrowinning-coupled CO_2 capture with energy-efficient absorbent regeneration: Towards practical application [J]. Chemical Engineering Journal, 2022, 427: 131981.

[25] WANG Chang-hong, JIANG Kai-qi, YU Hai, YANG Sheng-hai, LI Kang-kang. Copper electrowinning-coupled CO_2 capture in solvent based post-combustion capture [J]. Applied Energy, 2022, 316: 119086.

[26] WANG Chang-hong, LI Kang-kang, YU Hai, YANG Sheng-hai, JIANG Kai-qi. Electrochemical behavior of Cu-mediated electrowinning-coupled CO_2 capture [J]. Electrochimica Acta, 2022, 422: 140571.

[27] WANG Chang-hong, YANG Sheng-hai, CHEN Yong-ming, WANG Biao, HE Jing, TANG Chao-bo. Effect of bromide ions on the corrosion behavior of hafnium in anhydrous ethanol [J]. RSC Advances, 2015, 5: 34580−34587.

[28] AMIN M A, ABDEL REHIM S S. Pitting corrosion of lead in sodium carbonate solutions containing NO^{3-} ions [J]. Electrochimica Acta, 2004, 49: 2415−2424.

[29] AMIN M A. A newly synthesized glycine derivative to control uniform and pitting corrosion processes of Al induced by SCN− anions – Chemical, electrochemical and morphological studies [J]. Corrosion Science, 2010, 52: 3243−3257.

[30] WANG Chang-hong, YANG Sheng-hai, CHEN Yong-ming. Electrochemical behaviour of hydrogen evolution reaction on platinum in anhydrous ethanol containing tetraethyl-ammonium bromide [J]. Journal of Applied Electrochemistry, 2019, 49: 539−550.

[31] BOCKRIS J O M, REDDY A K N. Modern electrochemistry: Volume 2 [M]. Boston: Springer, 1970.

[32] MACDONALD J R. Impedance spectroscopy [J]. Annals of Biomedical Engineering, 1992, 20: 289−305.

[33] AMIN M A, ABD EL-REHIM S S, EL-SHERBINI E E F, MAHMOUD S R, ABBAS M N. Pitting corrosion studies on Al and Al−Zn alloys in SCN− solutions [J]. Electrochimica Acta, 2009, 54: 4288−4296.

[34] WANG Chang-hong, YANG Sheng-hai, YUAN Yi, CHEN Yong-ming, WANG Biao, HE Jing, TANG Chao-bo. Corrosion behavior of hafnium in anhydrous isopropanol and acetonitrile solutions containing bromide ions [J]. Transactions of Nonferrous Metals Society of China, 2017, 27: 1896−1906.

[35] ONSAGER L. Deviations from ohm's law in weak electrolytes [J]. The Journal of Chemical Physics, 1934, 2: 599−615.

非水四乙基氯化铵体系中电溶解耦合铪醇盐合成的电化学机理与动力学

李 帅[1]，杨声海[1]，陈永明[1]，唐朝波[1]，赖延清[1]，邓朝勇[2]，王长红[1]

1. 中南大学 冶金与环境学院，长沙 410083；
2. 稀美资源(广东)有限公司，清远 513000

摘 要：作为一种具有广泛应用前景的高效电合成技术，耦合电溶解的铪醇盐合成(EHS)基于铪溶解/乙醇脱氢的同时非均相反应以及溶液中 Hf^{4+}阳离子和烷氧阴离子的自发结合反应。为了阐明 EHS 过程的机制和动力学，通过电化学测试、扫描电镜、气相色谱和微观动力学模拟等手段，探究阳极铪溶解和阴极乙醇脱氢的电化学行为。结果表明，优选的支持电解质四乙基氯化铵(Et_4NCl)展现了钝化膜击穿与铪溶解协同的剧烈点蚀机制以及两段脱氢机制。为量化钝化膜击穿和铪点蚀的动力学参数，提取与钝化速率、钝化膜击穿敏感性和点蚀速率相关的 3 个指标，并通过建立微观动力学模型评估基于Et_4NCl体系的EHS工艺，其电能消耗为1.53~1.83 kW·h/kg $Hf(OC_2H_5)_4$。

关键词：铪醇盐合成；四乙基氯化铵；铪溶解；乙醇脱氢；电化学机理；电化学阻抗谱；微动力学模拟

(Edited by Xiang-qun LI)